Effect of aluminum modified mesoporous SBA-15 on surface properties and arsenic adsorption performance

Xueqing Liu[1,2] · Nengsheng Liu[1] · Xiang Li[1,2] · Yongming Luo[4] · Xiaoying Li[2,3] · Bo Hu[1,2] · Xintao He[1,2] · Chengwei Liu[1,2] · Sufang He[1,2]

Abstract

Aluminum-modified SBA-15 mesoporous materials (Al$_x$-SBA-15) were synthesized and used as the efficient adsorbents for As(V) removal. The effects of aluminum loading on the physicochemical properties such as microstructure, aluminum coordination environment and surface acidity of Al$_x$-SBA-15 were investigated carefully, and their correlation with adsorption performance was also studied in depth. After aluminum impregnation, aluminum oxide compounds with different coordination environments (AlO$_3$, AlO$_4$, AlO$_5$, and AlO$_6$), which contributed effectively to the active adsorption centers for As(V) removal, were successfully introduced onto the Al$_x$-SBA-15 samples with the maintenance of the ordered mesoporous structure of SBA-15. However, a decrease in specific surface area and pore volume of the sample was also caused by the increase of aluminum introduction. Moreover, an excessive increase of the aluminum loading led to the overlapping arrangement of aluminum oxides on the surface of SBA-15, which resulted in the obvious decline of the terminal Al–OH functional groups and acid centers. When the loading of aluminum was 10%, the positive and negative factors reached a balance, and then the highest adsorption capacity of 95.7 mg/g$_{A1}$ for As(V) was obtained. The adsorption kinetics of As(V) on Al$_x$-SBA-15 conformed to the pseudo-second-order kinetic equation and the intraparticle diffusion model, and the adsorption rate was controlled by both film diffusion and intraparticle diffusion. In conclusion, Al$_{10}$-SBA-15 is an efficient As(V) adsorbent that can treat actual arsenic-contaminated wastewater with the arsenate of 1.998 mg/L (and 1.242 mg/L) to reach drinking water standards.

Keywords Al-SBA-15 · Removal of arsenic · Alumina species · Surface acidity · Adsorption kinetics

1 Introduction

Arsenic is a toxic element in the environment, usually in the form of inorganic or organic compounds. Long-term exposure to arsenic can lead to various dangerous diseases such as cardiovascular disease, skin cancer, liver cancer, and lung cancer [1]. The main way of human exposure to arsenic is to intake arsenic-contaminated water and food [2]. Therefore, the health risk of drinking water caused by arsenic pollution in surface water has attracted wide attention. Given this, many organizations such as the United States Environmental Protection Agency (EPA) revised the standard for safe drinking water from the original 50 µg/L to 10 µg/L [3]. However, more than 200 million people worldwide still have access to drinking water containing arsenic above 10 µg/L [2].

At present, there are many technologies for treating arsenic-containing wastewater, such as methods of adsorption, precipitation, ion exchange, membrane separation,

✉ Nengsheng Liu
liunengshengms@163.com

✉ Sufang He
shucai1983@163.com

1 Faculty of Materials Science and Engineering, Kunming University of Science and Technology, Kunming 650093, Yunnan, China

2 Research Center for Analysis and Measurement, Kunming University of Science and Technology, Kunming 650093, Yunnan, China

3 Faculty of Metallurgical and Energy Engineering, Kunming University of Science and Technology, Kunming 650093, Yunnan, China

4 Faculty of Environmental Science and Engineering, Kunming University of Science and Technology, Kunming 650500, Yunnan, China

biological, extraction and flotation[4–6]. Compared with other methods, the adsorption process has the advantages of convenient operation, large processing capacity, high removal efficiency and little secondary pollution. It is suitable for low-concentration wastewater and advanced treatment of wastewater and thus is one of the most widely studied arsenic removal technologies in drinking water. The adsorbent is the most key factor in whether the adsorption is successful or not. Activated alumina is recommended by the EPA as one of the most suitable materials for arsenic removal [7] since it is rich in adsorption sites. The adsorption capacity of traditional activated alumina for arsenate can reach 15.9 mg/g, but the adsorption rate is very slow, which takes 170 h to reach the adsorption equilibrium [8]. Ghosh et al. synthesized γ-Al_2O_3 nanoparticles (NPs) adsorbent to remove As(III) and As(V) in solution [9]. The adsorption rate of γ-Al_2O_3 NPs was fast and the adsorption equilibrium could be reached after 2 h, but the adsorption capacity of As(III) and As(V) was only 769.23 µg/g and 1000 µg/g, respectively. Jiang et al. did a study on the dynamic adsorption of arsenic using activated alumina as adsorbent. When the initial arsenic concentration was 50 mg/L, the dynamic adsorption amount was 3.43 mg/g. Traditional alumina has the disadvantages of low adsorption capacity and slow adsorption rate, which may be related to its small specific surface area and uneven pore structure [10].

Mesoporous alumina with a large specific surface area, high porosity, well-organized pore structure and adjustable pore size can resolve those problems and help to obtain high adsorption capacity and fast adsorption rate. The mesoporous alumina prepared by Jin et al. using aluminum tri-sec-butoxide as the aluminum source could reach a specific surface area of 483 m^2/g and a maximum adsorption capacity of 61.3 mg/g for arsenate [11]. The adsorption capacity is 5 times higher than commercial activated alumina and the adsorption rate is 3.8 times higher. Li et al. synthesized highly ordered mesoporous alumina by sol–gel method and obtained the maximum arsenate removal of 19.8 mg/g[12]. Han et al. [13] synthesized mesoporous alumina with a specific surface area of 312 m^2/g using aluminum isopropoxide (AIP) as the aluminum source and obtained the maximum As(V) adsorption capacity of 36.6 mg/g. The equilibrium adsorption time is 3 h. Mixing yttrium nitrate solution with mesoporous alumina, the prepared mesoporous Y-Al binary oxide can increase the adsorption capacity of arsenic to 62.23 mg/g [14]. The adsorption performance of mesoporous alumina for arsenic is better than that of traditional alumina.

In addition, loading alumina onto the mesoporous carrier material with a high specific surface area is also a method to improve its adsorption performance. It was demonstrated that the introduction of aluminum and its oxides on mesoporous silica materials such as MCM-41, SBA-15 and KIT-6 not only preserved their large specific surface area and ordered mesoporous structure [15–17], but also produced a large number of acid sites and increased the surface acidity of the materials [18, 19], which had a positive impact on the adsorption performance. Boukoussa et al. [20] prepared Al-MCM-41 mesoporous material functionalized with aluminum for the adsorption of yellow dyes. The -OH group of the material increased with the increase of the Si/Al ratio, and a better adsorption effect was obtained. Glocheux et al. [21] used iron and aluminum oxides as metal coatings over mesoporous silica (OMS) and obtained a maximum arsenic adsorption capacity of 55 mg/g. Compared with other mesoporous silica materials, the SBA-15 material is more easily functionalized with functional groups, such as amines, thiol, sulfonic acid, and Al, Ce, Ti, etc. [22–25]. Moreover, SBA-15 materials have a larger specific surface area, more uniform pore size, better hydrothermal stability [26, 27], greater mechanical strength and more stable structures, and are often used as carriers in the synthesis of adsorbents [28, 29]. Wu et al. [30] prepared Al-SBA-15 materials for the adsorption of methylene blue by doping Al into SBA-15. The results showed that the Al-SBA-15 material had a good mesoporous structure, high specific surface area and highly dispersed Al species, which improved the adsorption capacity of methylene blue. Zhang et al. [31] synthesized AL-SBA-15 material at high temperature in the presence of inorganic salts, and the experimental results demonstrated that the sample has good hydrothermal stability as well as excellent selective adsorption, which is of practical application for the adsorption of biomolecules. Min Jang et al. [32] used the post-synthesis method to immobilize iron, aluminum and zinc oxides into mesoporous SBA-15 materials. The results showed that aluminum was the best incorporation metal compound. The adsorption capacity of arsenic on Al_{10}-SBA-15 is more than 2 times that of activated alumina, and the adsorption rate is 15 times that of activated alumina. In our previous studies [33], aluminum decorated SBA-15 was found to be an effective adsorbent for treating arsenate contaminated wastewater, and the adsorption behavior of As(V) onto Al-SBA-15 was investigated carefully under various experimental parameters. The results showed that the highly dispersed alumina on the adsorbent was the active adsorption site for arsenic removal, and the maximum adsorption capacity was 197.7 mg/g_{Al}. However, the changes in microstructure, surface properties of Al-SBA-15 adsorbent after aluminum loading, and the role of aluminum species in As(V) adsorption had not been addressed.

Therefore, in this study, different amounts of aluminum were loaded onto the highly ordered SBA-15 mesoporous materials (Al_x-SBA-15) by incipient wetness impregnation method using aluminum nitrate $Al(NO_3)_3 \cdot 9H_2O$ as the aluminum source to deeply investigate the effect of aluminum loading. XRD, N_2 adsorption–desorption, FT-IR, ^{27}Al NMR

and NH$_3$-TPD were used to characterize the microstructure, surface properties and distribution of aluminum species of Al$_x$-SBA-15. Also, different kinetic models were used to explore the adsorption performance and mechanism of As(V), and their relationships with microstructure, surface properties and aluminum species were understood. In addition, the adsorbent was applied to actual water samples to provide a theoretical basis for the design and development of the adsorbent in subsequent studies.

2 Experimental

2.1 Material

EO$_{20}$PO$_{70}$EO$_{20}$ (P123) was purchased from Sigma-Aldrich (America). Hydrochloric acid (HCl) was purchased from Shantou Xilong Chemical Factory Co. (China). Aluminum nitrate (Al(NO$_3$)$_3$•9H$_2$O), ethyl orthosilicate ((C$_2$H$_5$O)$_4$Si), disodium hydrogen arsenate heptahydrate (Na$_2$HAsO$_4$·7H$_2$O), nitric acid (HNO$_3$), sodium hydroxide (NaOH), thiourea (CH$_4$N$_2$S), and ascorbic acid (C$_6$H$_8$O$_6$) were purchased from Sinopharm Chemical Reagent Co. Ltd (China). The chemicals used were AR grade and the water used in the experiments was deionized.

2.2 Synthesis of SBA-15 and Al-SBA-15

SBA-15 was prepared using P123 as the template agent and TEOS as the silicon source according to the existing method [33]. Using aluminum nitrate as the aluminum source, aluminum was loaded onto SBA-15 by the incipient wetness impregnation method to modify SBA-15. A certain amount of SBA-15 carrier was weighed and immersed in aluminum nitrate solution with thorough stirring. After impregnation, the material was dried at 100 ℃ for 24 h and then placed in a muffle furnace. The aluminum-modified SBA-15 adsorbent was obtained by roasting at a rate of 2 °C/min to 400 °C for 3 h. The synthesized materials were denoted as Al$_x$-SBA-15, where x represented the mass fraction of Al (%).

2.3 Static adsorption experiment

The adsorption experiments in this study mainly used the static adsorption method, which was operated as follows. 0.2 g of adsorbent was placed in 50 mL of an As(V) solution with an initial concentration of 44.703 mg/L and the pH of the solution was 6.6 ± 0.1. Then, the adsorption of As(V) onto Al$_x$-SBA-15 was carried out under stirring (200 rpm) for a certain time. After adsorption, the mixture was centrifuged at the speed of 3000 rpm for 20 min to separate the solid adsorbent, and the concentration of As(V) in the supernatant was determined by inductively coupled plasma

optical emission spectrometry (ICP-OES, Prodigy, Leeman) and inductively coupled plasma mass spectrometry (ICP-MS, Elan DRC II, PE).

The adsorption performance of As(V) was mainly compared using removal rate and adsorption capacity, which were expressed by Eq. 2.1 and Eq. 2.2 as follows, respectively.

$$\eta = \frac{C_0 - C_t}{C_0} \times 100\%, \tag{2.1}$$

$$q = \frac{(C_0 - C_t) \times V}{m}, \tag{2.2}$$

where η (%) is the removal rate of As(V), C_0 (mg/L) is the initial concentration of As(V) in solution, C_t (mg/L) is the concentration of As(V) in solution at adsorption time t (min), q (mg/g) is the adsorption capacity of adsorbent for As(V), V (L) is the volume of adsorption solution, m (g) is the mass of adsorbent.

2.4 Characterization

Micromeritics-ASAP-2000 automatic adsorption instrument was used to determine the N$_2$ adsorption–desorption isotherms. The samples were first pretreated for 2 h under high vacuum (10^{-5} Torr) at 523 K, and then BET specific surface area and pore size distribution were measured by the N$_2$ adsorption method under liquid nitrogen (77 K). The specific surface area was calculated by Barrett-Emmett-Teller (BET) method, pore volume and pore size distribution were calculated by Berret-Joyner-Halenda (BJH) model.

Small-angle X-ray diffraction (XRD) patterns were measured on D/Max-1200 instruments using Cu Kα-radiation ($\lambda = 1.5406$, 40 kV, 30 mA). The scanning speed was 0.5°/min, and the scanning range was 0.5° ~ 8°. Wide-angle XRD patterns were measured on and Bruker D8 instruments using Cu Kα-radiation ($\lambda = 1.5406$, 40 kV, 200 mA). Wide-angle XRD patterns were recorded in the 2θ range from 20 to 80° and the scanning speed was 8°/min.

Fourier infrared (FT-IR) was conducted on a Bruker Vector22 spectrometer at a resolution of 2 cm^{-1}. The scanning range of the spectrum is 4000-400 cm^{-1}. ^{27}Al MAS NMR was performed on a Bruker DSX 300 solid-state NMR instrument with a voltage of 12 kHz.

Ammonia temperature-programmed desorption (NH$_3$-TPD) was performed on gas chromatography. The sample was first purged with He (40 mL/min) at 400 °C for 1 h, and then cooled to 100 °C under this condition. Then, the sample was treated with 10% NH$_3$ / He (60 ml/min) at 50 °C for 2 h to saturated NH$_3$, and then the sample was purged with He (60 mL/min) at 100 °C for 2 h to remove the physical adsorption of NH$_3$. Finally, the temperature was

ramped up to 1173 K at 10 K/min under He flow and cooled down in He gas until the desorption peak was out.

3 Results and discussion

3.1 Characterization of material

3.1.1 Structure of the material

Figure 1 shows the N_2 adsorption–desorption isotherms of SBA-15 and Al_x-SBA-15 samples. According to the IUPAC classification, the N_2 adsorption–desorption isotherms of pure SBA-15 and all Al_x-SBA-15 samples were classified as type IV [34], with a clear H1 hysteresis loop, which indicated that SBA-15 and all Al_x-SBA-15 adsorbents had a regular mesoporous structure with cylindrical channels.

Figure 1a shows that with the increase of aluminum loading, the volume of nitrogen adsorbed by Al_x-SBA-15 materials gradually decreases, and the position of abrupt relative partial pressure P/P_0 on the adsorption line moves to the lower P/P_0 direction. These phenomena indicated that the pore volume and specific surface area of Al_x-SBA-15 samples decreased with the increase of aluminum loading, and the mesoporous pore size and the regularity of mesoporous structure also decreased. As the aluminum content increased, the number of aluminum atoms carried on the surface of SBA-15 increased, and when the single-layer distribution could not fully satisfy the aluminum loading, the

aluminum atoms began to be distributed in multiple layers. It might lead to the blockage of SBA-15 pores and reduction of pore volume and specific surface area. The pore size distribution on SBA-15 was narrow, with an average pore size of about 7.6 nm. Similar to the previous literature [35, 36], the Al_x-SBA-15 sample showed a binary pore distribution, as shown in Fig. 1b. The inhomogeneous loading of aluminum led to a slight collapse of the SBA-15 structure, which allowed the blockage of partial pores and promoted the formation of smaller new pores.. There were two pores on the surface of Al_x-SBA-15, which were located at about 6.0 nm and 3.5 nm, respectively. With the increase of aluminum loading, the intensity of the small pore peak at about 3.5 nm increased, while the intensity of the large pore peak at about 6.0 nm decreased. It indicated that as the loading of aluminum increased, the number of aluminum atoms distributed in multiple layers increased, and the transformation of large pores to small pores became more and more obvious. Therefore, the degree of pore blockage on SBA-15 became more and more serious with the increase of aluminum loading.

Table 1 shows the structural parameters of SBA-15 and Al_x-SBA-15 samples. ICP analysis was performed to determine the content of Al on Al_x-SBA-15 samples, the actual aluminum loadings on the Al_x-SBA-15 (x = 5,7.5,10,15) samples were 4.7%, 6.2%, 7.4%, and 11.2%, respectively. It indicated that aluminum had been successfully loaded in the mesopores of SBA-15. The specific surface area and pore volume of SBA-15 decreased rapidly with the addition

Fig. 1 The N_2 adsorption–desorption isotherms and the BJH pore size distributions of SBA-15 and Al_x-SBA-15 with different loading of aluminum
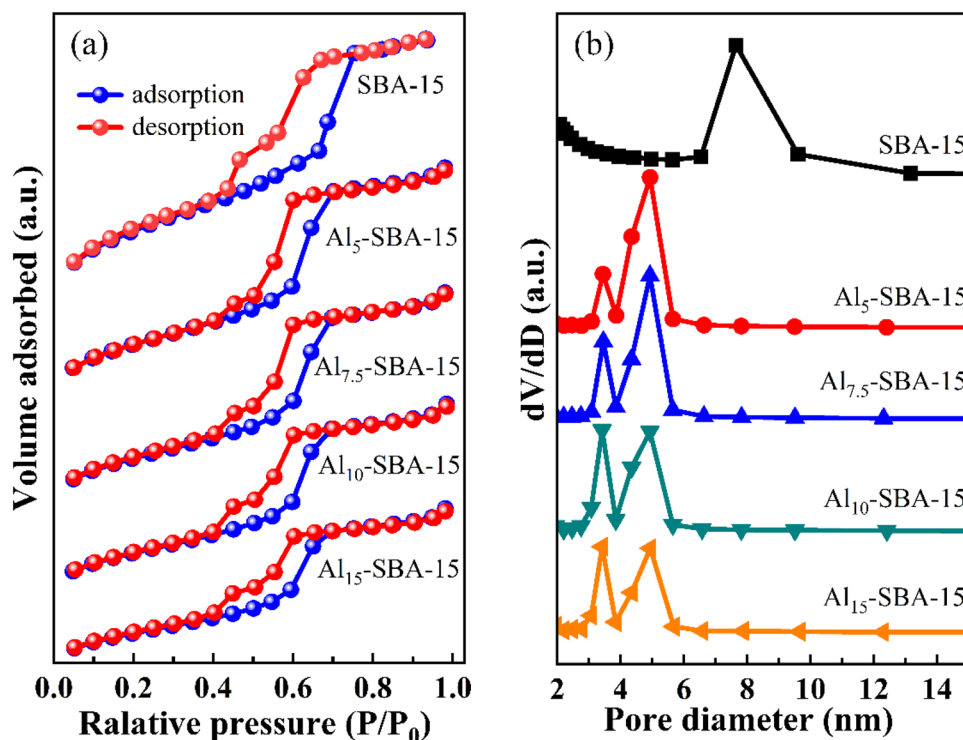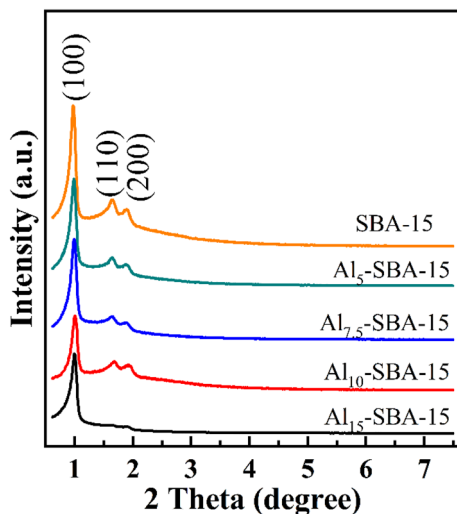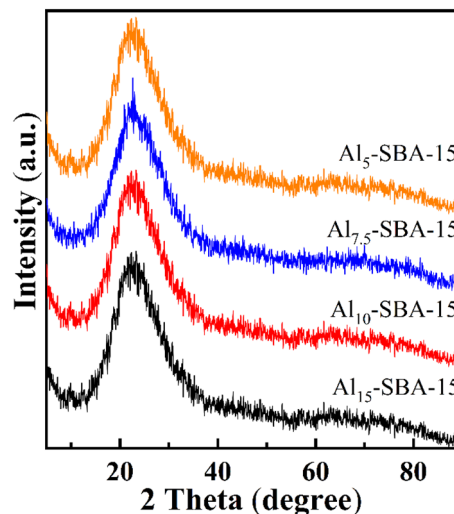
Table 1 Structural parameters of SBA-15 and Al$_x$-SBA-15

Adsorbent	SBA-15	Al$_5$-SBA-15	Al$_{7.5}$-SBA-15	Al$_{10}$-SBA-15	Al$_{15}$-SBA-15
BET surface area (m^2/g)	658	521	473	404	346
Pore volume (cm^3/g)	0.98	0.69	0.65	0.60	0.54
Mean pore diameter (nm^a)	6.1	5.7	5.7	5.4	5.1
Content of Al (%^{b})	0.0	4.7	6.2	7.4	11.2

^{a}Average pore size $= 4 \times$ pore volume/S_{BET}

^{b}Data were measured using ICP-OES

Fig. 2 The small-angle XRD patterns of SBA-15 and Al$_x$-SBA-15 with different loading of aluminum

Fig. 3 The wide-angle XRD profiles of Al$_x$-SBA-15 with different loading of aluminum

of aluminum. When the loading of aluminum was 5%, the specific surface area of SBA-15 decreased rapidly from 658 to 521 m^2/g, and the pore volume decreased from 0.98 to 0.69 cm^3/g. When the loading of aluminum was increased to 15%, the specific surface area and pore volume of Al$_x$-SBA-15 samples were only 346 m^2/g and 0.54 cm^3/g. Obviously, with the increase of Al loading, the specific surface area, pore volume and average pore diameter of the samples gradually decreased, and the degree of pore blockage on SBA-15 was becoming more and more serious.

SBA-15 and Al$_x$-SBA-15 samples were characterized by small-angle XRD technology to understand the changes in their microstructure after Al's introduction. The results are shown in Fig. 2. The small-angle XRD curves of SBA-15 and Al$_x$-SBA-15 samples had three diffraction peaks from 0.5 to 2°: a strong peak at about 0.98° and two weak peaks at about 1.7° and 1.9°, corresponding to (100) (110) and (200) faces of SBA-15, respectively. These diffraction peaks were related to the 2-D hexagonal p6mm symmetry of SBA-15 material[37], and their existence indicated that the mesoporous structure of SBA-15 was maintained after the addition of aluminum. However, with the increase in aluminum loading, the intensities of the three diffraction peaks (100), (110) and (200) were significantly weakened. Especially for the Al$_{15}$-SBA-15 sample, the two peaks of the (110) and (200) peaks were very weak, and their existence was almost not observed. These phenomena indicated that the increase in aluminum loading increased the number of aluminum atoms per unit volume of SBA-15, resulting in the blockage of mesoporous channels and the decrease of structural regularity of SBA-15 to a certain extent[38]. Moreover, with the increase of aluminum loading, the ratio of d$_{200}$ peak intensity to d$_{110}$ peak intensity on Al$_x$-SBA-15 samples also increased. It was probably due to the increasing number of aluminum atoms covering the surface of SBA-15, which gradually thickened the pore wall of the SBA-15 mesoporous pore channel [39, 40].

The wide-angle XRD patterns of Al$_x$-SBA-15 samples in Fig. 3 show that no other substance, except for a large amorphous SiO$_2$ diffraction peak at about 25°, is detected on all Al$_x$-SBA-15 samples. Whether the loading of aluminum was 5% or 15%, the presence of alumina was not detected in the samples, indicating that the aluminum oxides on the Al$_x$-SBA-15 samples were highly dispersed.

In this study, FTIR technique was used to characterize the nitrate group of Al$_{10}$-SBA-15 after drying at 100 °C to

determine indirectly whether the incorporation of aluminum nitrateis on SBA-15 is successful. As shown in Fig. 4, the IR peaks at 1620 cm^{-1} and 1376 cm^{-1} in the aluminum nitrate standard were attributed to the asymmetric and symmetric stretching vibrations of nitrate ions [41], respectively. The bands at 1631 cm^{-1} belonged to the vibrational peak of adsorbed water [42], which did not appear on the unbaked Al$_{10}$-SBA-15, was due to the drying of Al-SBA-15 at 100 °C. The bands at 1084 cm^{-1}, 805 cm^{-1} and 461 cm^{-1} belonged to asymmetric stretching vibration, symmetric stretching vibration and bending vibration of the Si–O-Si bond[40, 43, 44], respectively. In the unbaked Al$_{10}$-SBA-15 precursor material, the asymmetric stretching vibration peak of nitrate ion at 1620 cm^{-1} shifted to 1639 cm^{-1}, and the symmetric stretching vibration peak of nitrate at 1376 cm^{-1} shifted to
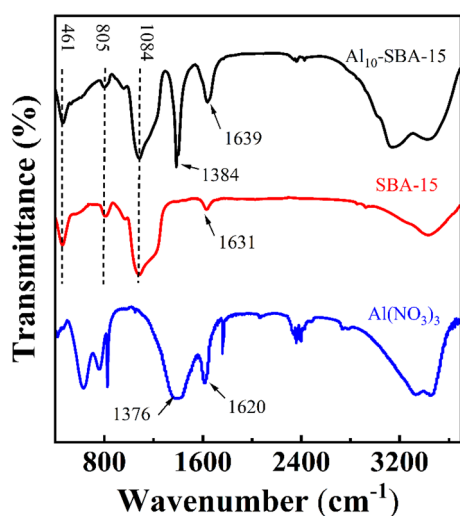
1384 cm^{-1}, which may be due to the interaction of aluminum nitrate with the SBA-15 carrier [45]. FT-IR results showed that aluminum nitrate was successfully loaded on SBA-15 by the incipient wetness impregnation method.

Then, the FT-IR spectra of calcined Al$_x$-SBA-15 adsorbents are compared and the results are shown in Fig. 5. No stretching vibrations of nitrate ions had been detected by FT-IR spectra, indicating that the aluminum nitrate precursor salt had been completely decomposed after calcination at 400 °C to successfully form alumina species on Al$_x$-SBA-15 material. The intensity of the three characteristic peaks of the Si–O–Si bond decreased significantly with the increase in aluminum loading.. The broad absorption band at 3432 cm^{-1} belonged to the stretching vibration peak of the -OH group[46]. In addition, the peak at 967 cm^{-1} on the SBA-15 sample was attributed to the stretching vibration peak of silanol groups (Si–OH) [46, 47], which disappeared after the loading of aluminum. The above situation indicates that with the increase of aluminum loading, and the silicon atoms on the sample surface are covered or replaced by more and more aluminum atoms, thus the content of Si–O-Si bonds on the sample surface decreases and the Si–OH groups disappear.

The aluminum coordination environment of all the Al$_x$-SBA-15 samples was characterized by ^{27}Al MAS NMR and the results were shown in Fig. 6. Three peaks at 6.2 ppm, 39.5 ppm and 62.7 ppm were detected on all the Al$_x$-SBA-15 samples, which correspond to octahedral aluminum (AlO$_6$)[17, 48], penta coordinated aluminum (AlO$_5$)[39] and tetra coordinated aluminum (AlO$_4$)[17], respectively. With the increase in aluminum loading, the intensities of these three peaks increased, which indicated that the contents of AlO$_6$, AlO$_4$ and AlO$_5$ increased with the increase in aluminum loading. It was worth noting that the growth ranges of these three peaks were different:

Fig. 4 The FT-IR profiles of aluminum nitrate and precursor of Al$_{10}$-SBA-15 before calcination

Fig. 5 The FT-IR profiles of SBA-15 and Al$_x$-SBA-15 with different loading of aluminum
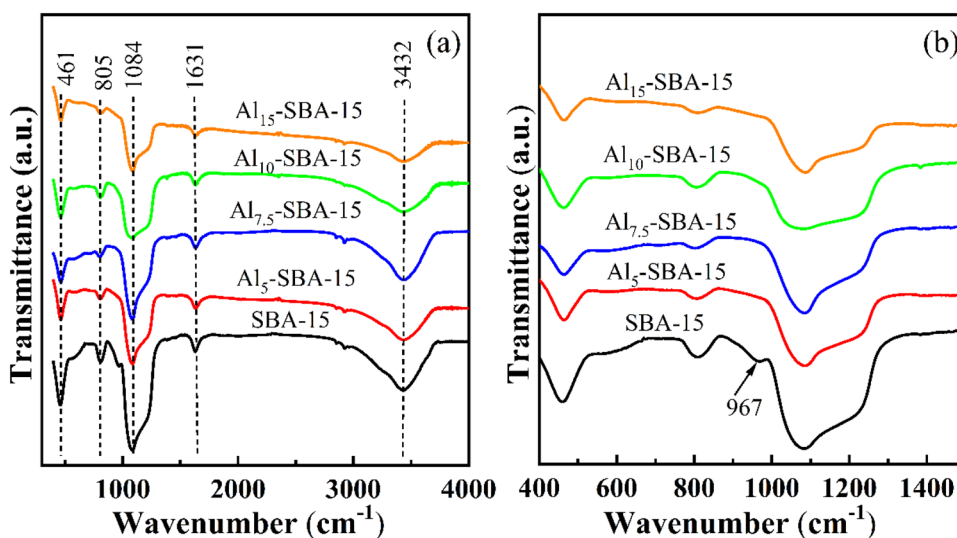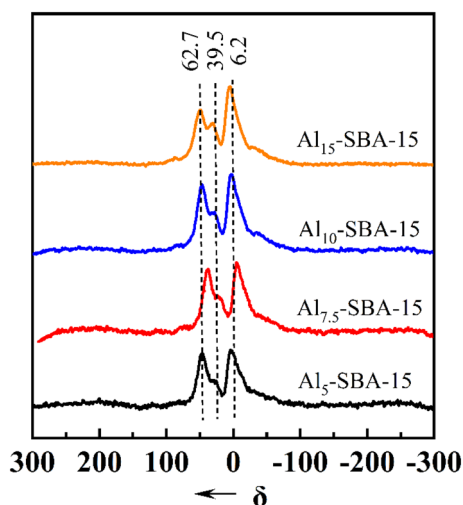
Fig. 6 The ^{27}Al MAS NMR profiles of Al_x-SBA-15 with different loading of aluminum

Fig. 7 The NH_3-TPD profiles of Al_x-SBA-15 with different loading of aluminum.3.2 Adsorption performance of Al_x-SBA-15

when the aluminum loading was low (from 5 to 7.5%), the content of AlO_6 and AlO_4 increased obviously with the aluminum loading. When the aluminum loading was high (from 10 to 15%), the content of AlO_5 increased more obviously with the aluminum loading. The ratio of the total amount of AlO_5 and AlO_4 to the total amount of AlO_6 also increased with the increase of aluminum loading. These phenomena might be caused by the following reasons: Excessive increase of aluminum loading led to the overlapping arrangement of aluminum oxide compounds on the surface of SBA-15, resulting in excessive overlapping of terminal Al–OH functional groups[39]. These excessively overlapping terminal Al–OH functional groups might dehydrate with the adjacent -OH groups, which made the aluminum transition to a low coordination environment.

On the one hand, these aluminum oxides produced terminal Al–OH groups on the surface of the adsorbent, which could adsorb uncharged arsenic acid molecules by hydrogen bonding, or could form positively charged $[Al–OH_2]^+$ functional groups after protonation, thus adsorbing negatively charged As(V) in solution by electrostatic action. On the other hand, they produced different acidic sites. According to the literature, AlO_5 had an empty hybridization orbital on the aluminum atom, which could attract external lone pair electrons to form Lewis acidic sites [49]. The Al–O–Si bond on AlO_4 could form a bridged -OH, resulting in Brønsted acidic sites [50].Also, the terminal Al–OH groups of AlO_5 and AlO_6 generated weak acidic sites on the surface. It was anticipated that different surface acid sites would been formed on the surface of Al_x-SBA-15 samples and then interacted with As(V) in aqueous solutions and removed it.

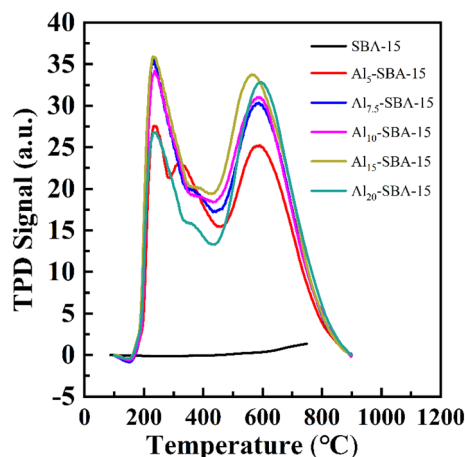### 3.1.2 Surface acidity

To examine the variation of surface acidity with the increasing amount of aluminum, NH_3-TPD was used to characterize Al_x-SBA-15 in this work, as shown in Fig. 7. As expected, there was no obvious NH_3 desorption peak on the NH_3-TPD curve of pure SBA-15, indicating that SBA-15 had no acidity. In contrast, some obvious NH_3 desorption peaks appeared after aluminum loading, and the area of NH_3 desorption peak on the NH_3-TPD curves of Al_x-SBA-15 increased with the loading of aluminum from 5 to 15%, indicating that the total number of surface acidic sites of Al_x-SBA-15 increased with the loading of aluminum. The total amount of acidic sites on the surface of the Al_{15}-SBA-15 sample reached a maximum when the aluminum loading reached 15%, and then the NH_3 desorption peak area on the NH_3-TPD curve decreased with the increase of the aluminum loading to 20%.

Further comparing several NH_3-TPD curves in Fig. 7, it can also be found that the peak area of strong acid sites (about 400 to 900 °C) did not decrease significantly under high aluminum loading, while weak acid sites (about 100 to 200 °C) showed a significant decreasing trend. The weak acid part was generated by the terminal Al–OH groups of AlO_5 and AlO_6 on the surface. The strong acid centers were generally attributed to Lewis acid sites formed by attracting foreign lone pair electrons to the orbitals above AlO_5 and AlO_3 (in NH_3-TPD characterization, the samples should be calcined in air at 400 °C for 1 h, which may lead to the formation of AlO_3), and the intermediate temperature peaks (about 300 to 400 °C) were attributed to Brønsted acid sites.

Based on the above characterization results, the different alumina species produced different acid sites over Al_x-SBA-15, thus, the surface acidity increased with aluminum loading. However, an excessive increase in aluminum loading (from 15 to 20%) could lead to the overlapping

arrangement of aluminum oxides with different coordination environments. Moreover, the decrease in specific surface area, pore volume and structural regularity with the increase of aluminum loading, which was confirmed by N_2 adsorption–desorption isotherms and small-angle XRD characterization results, could make the overlapping arrangement of aluminum oxides more serious, which eventually led to the further reduction of the total acid sites on the surface of Al_x-SBA-15 samples. Combined with the above ^{27}Al MAS NMR characterization results, when the aluminum loading was relatively high, the specific surface area and pore volume of Al_x-SBA-15 samples were small, and the overlap distribution of terminal Al–OH groups on the surface aluminum oxide compounds was obvious. In the case of dense distribution, it could also undergo dehydration reactions with the adjacent -OH groups, reducing the number of available terminal Al–OH groups and thus leading to a decrease in the weakly acidic centers. With the increase of the total amount of AlO_4 and AlO_5, the total amount of Lewis acidic centers due to Brønsted acidic centers and empty hybridization orbitals also increased. In addition, the total amount of AlO_3 formed in the heat treatment case also increased, which further increased the number of Lewis acidic sites. Under the combined effect of these factors, the number of medium and strong acidic sites became relatively high, so the ratio between the number of strong acidic sites and the number of weak acidic sites also increased with the increase of aluminum loading.

3.1.3 Effect of aluminum loading on As(V) adsorption

Figure 8 shows the effects of different aluminum loadings on As(V) adsorption. Obviously, SBA-15 had no adsorption capacity for As(V), while the addition of aluminum significantly improved the removal efficiency of adsorbent for As(V). For Al_5-SBA-15, $Al_{7.5}$-SBA-15, Al_{10}-SBA-15 and Al_{15}-SBA-15 samples, the equilibrium adsorption capacities of As(V) were 5.40 mg/g and 7.66 mg/g, 9.57 mg/g and 8.91 mg/g, respectively. It indicated that the loading of aluminum was not the higher the better, and its optimal value was 10%. The changing trend of adsorption rate was similar to that of adsorption capacity, but for the above four adsorbents, the equilibrium time of As(V) adsorption was 960 min.

Combined with the analysis of the above characterization results, it can be inferred that the surface of pure SBA-15 was filled with Si–OH groups, which were electrically neutral and chemically inert, so they generally did not have adsorption properties for As(V). The increase in aluminum loading had two opposite effects on the Al_x-SBA-15 samples. On the one hand, the addition of aluminum maintained the mesoporous structure of SBA-15 materials and introduced alumina compounds with different coordination
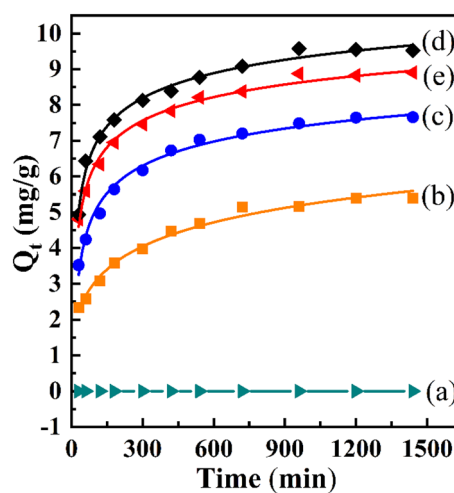

Fig. 8 The effect of Al loading on the capacities of As(V) removal, a: SBA-15; b: Al_5-SBA-15; c: $Al_{7.5}$-SBA-15; d: Al_{10}-SBA-15 and e: Al_{15}-SBA-15. Experimental conditions: initial concentration = 44.703 mg/L, solution volume = 50 mL, contact time = 960 min, pH = 6.6 ± 0.1, adsorption temperature RT and adsorbent dosage 0.2 g

environments. These alumina compounds produced a large number of terminal Al–OH functional groups and different acidic centers, so that the number of active adsorption centers was effectively improved. On the other hand, the specific surface area of the Al_x-SBA-15 samples was reduced, and the pores were blocked. The excessive increase of aluminum loading also led to the overlapping arrangement of aluminum oxides in different coordination environments, which reduced the number of active adsorption centers. When the aluminum loading was 10%, the effects of these two aspects reached dynamic equilibrium. At this time, Al_{10}-SBA-15 showed the optimal performance in the adsorption of As(V), and then the highest adsorption capacity of 95.7 mg/g_{Al} for As(V) was obtained.

3.1.4 Adsorption kinetics

The control mechanism of the adsorption process is usually investigated by analyzing the adsorption kinetics. In this work, pseudo-first-order and pseudo-second-order kinetic models were used to analyze the kinetic characteristics of As(V) adsorption on Al_x-SBA-15 adsorbents.

The pseudo-first-order kinetic rate equation is as follows:

$$\ln(Q_e - Q_t) = \ln Q_e - K_1 \cdot t, \tag{3.1}$$

where Q_e (mg/g) and Q_t (mg/g) are the equilibrium adsorption capacity and the adsorption capacity at time t (min), respectively, t (min) is the adsorption time, K_1 (min^{-1}) is the rate constant of the quasi-first-order kinetic equation. With

time t as the horizontal coordinate and $\ln(Q_e-Q_t)$ as the vertical coordinate, a linear fit can be made to the experimental data, and from the slope and intercept, the corresponding kinetic parameters.

The pseudo-second-order kinetic equation is as follows:

$$\frac{t}{Q_t} = \frac{1}{K_2 Q_e^2} + \frac{1}{Q_e}t, \qquad (3.2)$$

where K_2 (g mg^{-1} min^{-1}) is a pseudo-second-order rate constant, the meanings of other symbols are the same as those in formula 3.1. Similarly, with time t as the abscissa and t/Q_t as the ordinate, the experimental data are linearly fitted, and the corresponding kinetic parameters can be calculated from the slope and intercept.

The pseudo-first-order kinetic and pseudo-second-order kinetic linear simulation results of the adsorption data of As(V) in an aqueous solution for Al$_x$-SBA-15 samples with different aluminum loadings are shown in Fig. 9 and Fig. 10, respectively, and the corresponding kinetic parameters obtained from the linear simulation results are shown in Table 2. By comparing the two groups of parameters in Table 2, it can be inferred that the linear regression coefficient R^2 of the pseudo-second-order kinetics of As(V) adsorption on Al$_x$-SBA-15 is greater than 0.99, while the R^2 of the linear fitting curve of the first-order kinetics is between 0.964 and 0.982, and the deviation from 1 is relatively large. Furthermore, the theoretical adsorption capability computed by the pseudo-second-order kinetic linear fitting curve is closer to the experimental real value. These linear fitting curves and kinetic parameters further illustrate that the adsorption kinetics of As(V) on Al$_x$-SBA-15 with different aluminum loadings belongs to
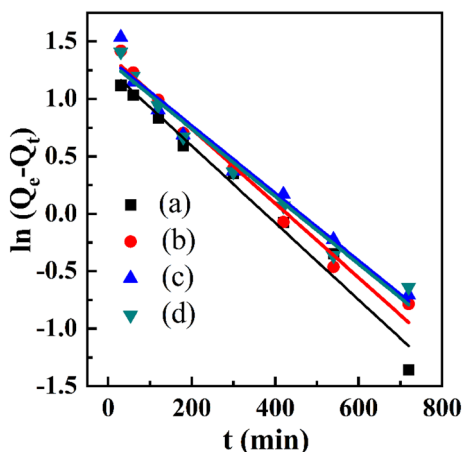

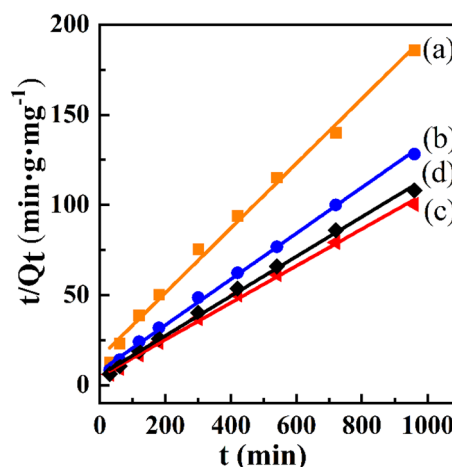**Fig. 10** Linearized plots of pseudo-second-order kinetic model for As(V) adsorption on Al$_x$-SBA-15. a: Al$_5$-SBA-15; b: Al$_{7.5}$-SBA-15; c: Al$_{10}$-SBA-15 and d: Al$_{15}$-SBA-15

pseudo-second-order kinetics. That is, the adsorption process is dominated by chemisorption[51].

3.1.5 Intraparticle diffusion model

The pseudo-first-order kinetics and pseudo-second-order kinetic models described above cannot be used to investigate the rate-determining step of the adsorption process, which is important for the study of adsorption systems. In general, the rate of an adsorption process may be determined by different stages, including membrane diffusion and pore diffusion, or controlled by both. To investigate which process is the rate-determining step of the adsorption process, this paper uses the internal diffusion model to analyze the experimental data.

The expression of the internal diffusion equation is:

$$Q_t = K_3 t^{1/2} + C, \qquad (3.3)$$

where K_3 (mg/g/min$^{1/2}$) is the internal diffusion rate constant, C (mg/g) is constant, other symbols represent the agreement in Eq. 3.1. With $t^{1/2}$ as the abscissa and Q_t as the ordinate, the experimental data were piecewise linearly fitted, and the relevant internal diffusion kinetic parameters can be calculated from the obtained fitting curve.

The linear simulation results of the intramolecular diffusion kinetics for the adsorption data of As(V) in aqueous solution by Al$_x$-SBA-15 with different aluminum loadings are shown in Fig. 11, and the intraparticle diffusion kinetic parameters derived from the linear simulation results are shown in Table 3.

Figure 11 shows that for Al$_x$-SBA-15 adsorbents with different aluminum loadings, the linear simulation curves of intraparticle diffusion kinetics can be divided into three

Fig. 9 Linearized plots of pseudo-first-order kinetic model for As(V) adsorption on Al$_x$-SBA-15. a: Al$_5$-SBA-15; b: Al$_{7.5}$-SBA-15; c: Al$_{10}$-SBA-15 and d: Al$_{15}$-SBA-15

Table 2 Pseudo-first-order and pseudo-second-order kinetic parameters for As(V) adsorption on Al_x-SBA-15

Adsorbent	$q_{e(exp)}$ (mg/g)	pseudo-first order			pseudo-second order			
		K_1 (min^{-1})	$q_{e\,(cal)}$ (mg/g)	R^2	K_2 (g/mg min)	$q_{e(cal)}$ (mg/g)	v_0 (mg/g min)	R^2
Al_5-SBA-15$_{400}$	5.40	0.0034	3.54	0.975	0.0021	5.57	0.065	0.993
$Al_{7.5}$-SBA-15$_{400}$	7.66	0.0033	4.00	0.981	0.0020	7.87	0.127	0.998
Al_{10}-SBA-15$_{400}$	9.57	0.0030	3.88	0.964	0.0022	9.78	0.207	0.997
Al_{15}-SBA-15$_{400}$	8.91	0.0030	3.78	0.972	0.0022	9.10	0.182	0.997

phases, and the first phase starts from the origin and ends at 30 min. The start and end times of the second and third phases vary with the aluminum loading, as shown in Table 3. The As(V) in the solution first diffuse from the solution to the external surface of the adsorbent by film diffusion and were rapidly adsorbed on the external surface. As the adsorption proceeds, the active adsorption sites on the external surface had reached adsorption saturation and could no longer adsorb As(V). At this time, the As(V) that had reached the external surface were forced to enter the pore channels of the Al_x-SBA-15 adsorbents by intraparticle diffusion and then rapidly adsorbed on the interior surface. For the same adsorbent, as the adsorption proceeds, the slope of the linear fitting curve of the intraparticle diffusion in the three stages became smaller and smaller ($K_{3,1} > K_{3,2} > K_{3,3}$), while the intercept became larger and larger ($C_1 < C_2 < C_3$). It indicated that on the same adsorbent, as the adsorption time increases, the intraparticle diffusion rate gradually decreased, while the contribution of film diffusion to the rate-determining step increased [1]. This could be caused by the following two aspects. On the one hand, with the adsorption process, the number of As(V) species in the solution decreased, the adsorption kinetics decreased, and the intraparticle diffusion rate decreased. On the other hand, with the progress of adsorption, the As(V) species adsorbed on the adsorbent became more and more, and it had a repulsion with the As(V) species in the solution, which made the film diffusion more and more difficult. At this time, the influence of film diffusion on the rate-determined step became greater.
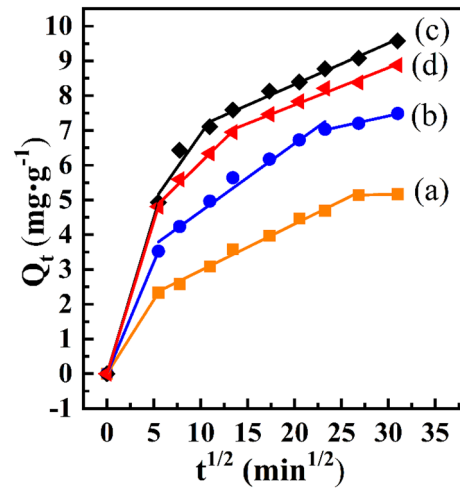

Fig. 11 Intraparticle diffusion plots for As(V) adsorption on Al_x-SBA-15. a: Al_5-SBA-15; b: $Al_{7.5}$-SBA-15; c: Al_{10}-SBA-15 and d: Al_{15}-SBA-15

The slope and intercept of the linear fit curve of diffusion within the three stages were generally increasing when the aluminum loading was from 5 to 10%. It indicated that the diffusion rate of As(V) on the adsorbent gradually increased. The diffusion rate decreased overall when the aluminum loading was from 10 to 15%. From the previous characterization results, it is known that the number of active sites of the adsorbent is larger when the aluminum loading is higher. As(V) species were quickly adsorbed on the external surface of the adsorbent, followed by intraparticle diffusion.

Table 3 Intraparticle diffusion kinetic parameters for As(V) adsorption on Al_x-SBA-15

Adsorbent	Intraparticle diffusion											
	Time region (min)	$K_{3,1}$	C_1	R^2_1	Time region (min)	$K_{3,2}$	C_2	R^2_2	Time region (min)	$K_{3,3}$	C_3	R^2_3
Al_5-SBA-15	0~30	0.4259	0	1.0	30~1200	0.1335	1.6376	0.9917	1200–1440	0.0070	4.9518	1.0
$Al_{7.5}$-SBA-15	0~30	0.6431	0	1.0	30~960	0.1949	2.7234	0.9727	960–1440	0.0594	5.6354	0.9816
Al_{10}-SBA-15	0~30	0.9003	0	1.0	30–120	0.3849	3.0542	0.8094	120–1440	0.1185	5.9521	0.9869
Al_{15}-SBA-15	0~30	0.8776	0	1.0	30–180	0.2645	3.4363	0.9891	180–1440	0.1069	5.5962	0.9817
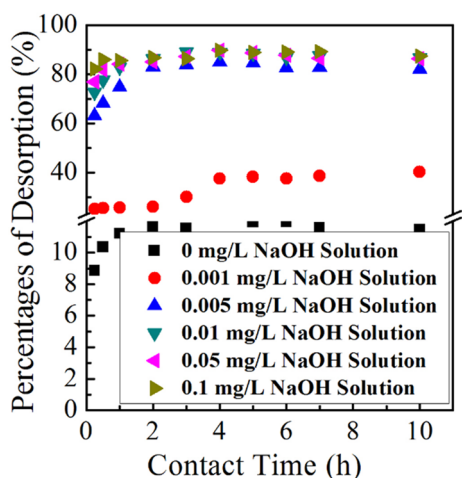
Fig. 12 The desorption percentage of Al$_{10}$-SBA-15 after saturation under different concentrations of NaOH solution

Fig.13 Removal rate of As(V) on Al$_{10}$-SBA-15 under different regeneration cycles

However, the mesoporous channels of the adsorbent collapsed with the increase of aluminum loading, and the specific surface area and pore volume decreased. The collapse of pores and the decrease of pore volume were not conducive to the smooth passage of As(V) in the pores, so the intraparticle diffusion was more limited than the film diffusion, which was the rate-determining step in the first stage. Then, as the adsorption proceeded, the number of As(V) species in the solution decreased, and more and more As(V) species were adsorbed on the external surface of the adsorbent or the pores close to the external surface. This increased the rejection between the external surface and the As(V) species in the solution, making the film diffusion more and more difficult. At this time, the effect of film diffusion on rate determination steps became greater. When the loading of aluminum was higher, the number of aluminum oxide compounds was larger, that is, the number of active adsorption sites was larger. This meant that the amount of As(V) adsorbed on the interior surface by entering the pores was less, and the time to reach uniform adsorption was relatively short. Therefore, with the increase in aluminum loading, the second stage of As(V) adsorption on Al$_x$-SBA-15 lasted shorter and shorter.

For Al$_x$-SBA-15 samples with different aluminum loadings, considering the entire adsorption process, the intraparticle diffusion curves of As(V) adsorption in an aqueous solution were not linear, indicating that film diffusion and intraparticle diffusion jointly determined the adsorption rate of As(V) on Al$_x$-SBA-15 [52].

3.1.6 Desorption study

The desorption of As(V) from Al$_{10}$-SBA-15 adsorbent was also studied using NaOH solution as desorption agent, and
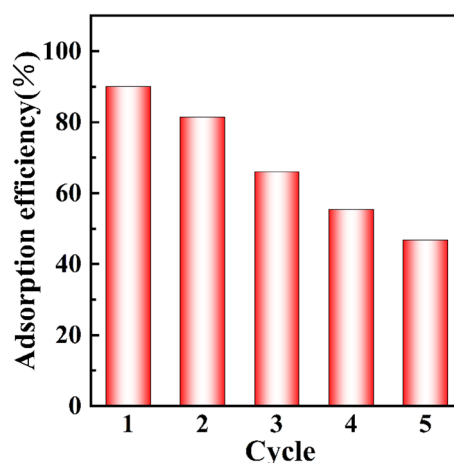
the results were shown in Fig. 12. The desorption efficiency of As(V) from Al$_{10}$-SBA-15 increased with the increase of NaOH concentration in the desorption solution. Especially when the concentration of NaOH solution increased from 0.001 to 0.005 mg/L, the desorption efficiency increased significantly from 39 to 84%. When the concentration increased from 0.005 to 0.1 mg/L, the desorption efficiency increased slowly from 84 to 90%. The effect of desorption time showed that the rate of desorption of Al$_{10}$-SBA-15 material in NaOH solution was very fast. For the solution with a higher NaOH concentration ($\geq$ 0.01 mg/L), more than 80% of the total As(V) desorption amount had been completed within 15 min. When the NaOH concentration was 0.005 mg/L, the As(V) desorption amount reached more than 70% within 15 min. The desorption was completed after 4 h, and the desorption efficiency reached 90%. The desorption generated a high concentration of As(V) solution, which provided the possibility for the subsequent resource utilization of arsenic pollution.

3.2 Reusability of Al-SBA-15

The recycling of Al-SBA-15 has been investigated, and the results were shown in Fig.13. To investigate the reusability of Al-SBA-15, 0.2 g of Al$_{10}$-SBA-15 material was first adsorbed in 50 ml of As(V) solution with an initial concentration of 44.703 mg/L for 16 h. After the adsorption was completed, the adsorption efficiency was calculated , which was part of the first cycle. Then the adsorbate was desorbed in a 0.1 mg/L NaOH solution for 4 h. The desorbed adsorbate was dried at 90 °C. After the completion of drying, the above steps were repeated for adsorption again. There was a loss of mass of adsorbed mass during this process, and for the fifth cycle, the mass of adsorbed mass was only 0.12 g.
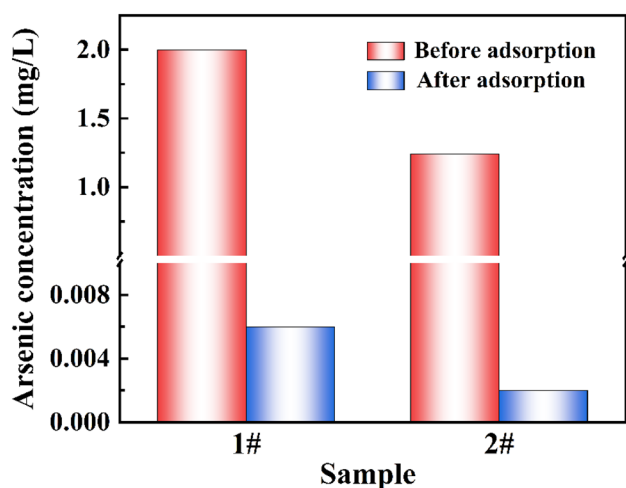
Fig. 14 The removal of As(V) in real contaminated natural water on Al_{10}-SBA-15. Experimental conditions: solution volume = 50 mL, adsorption temperature RT and adsorbent dosage 0.2 g

According to Figure 13, the adsorption efficiency of the Al_{10}-SBA-15 sample for As(V) decreased with the increase in the number of cycles. In the fifth cycle, the adsorption efficiency decreased to 46.8%. The decrease in adsorption efficiency was partly due to the decrease in adsorption capacity of the adsorbent itself, but more mainly due to the excessive mass loss of the Al_{10}-SBA-15 sample. It indicated that the Al_{10}-SBA-15 sample had good adsorption capacity and reproducibility, but its mass loss upon reuse was a problem for use in practical applications.

3.3 Application in actual polluted natural water

To investigate the removal ability of Al_{10}-SBA-15 adsorbent for As(V) from actual water samples, two different actual natural water samples contaminated with arsenic were taken for adsorption experiments, as shown in Fig. 14. The content of co-existing anions in the actual water samples was also measured in this work, and the results were listed in Table 4.

The Al_{10}-SBA-15 adsorbent had a good removal effect for As(V) in these two polluted actual water samples. For the 1# actual water sample with an initial As(V) concentration of 1.998 mg/L, the concentration of As(V) was reduced to 6 µg/L after the adsorption treatment of Al_{10}-SBA-15. For the 2# actual water sample with an initial As(V) concentration of 1.242 mg/L, the concentration of As(V) was reduced to 2 µg/L after the adsorption treatment of Al_{10}-SBA-15. The

concentrations of As in drinking water were lower than the maximum limit specified by WHO. The presence of SO_4^{2-}, NO^{3-}, Cl^-, PO_4^{3-}, F^- and other anions in the actual water sample competed with the As(V) species for the active adsorption center and resulted in a decrease in the adsorption effect of As(V) on the adsorbent. The Al_{10}-SBA-15 sample was still effective in treating arsenic-contaminated water under such circumstances, indicating that it can be used to treat actual arsenic-contaminated natural water bodies.

4 Conclusion

In this work, Al-SBA-15 mesoporous adsorbent materials with different aluminum loadings (5%, 7.5%, 10%, 15%) were prepared and used as the efficient adsorbents for As(V) removal. The increase in aluminum loading had two opposite effects on the Al_x-SBA-15 samples. On the one hand, aluminum oxide compounds with different coordination environments (AlO_3, AlO_4, AlO_5, and AlO_6) were successfully introduced to the Al_x-SBA-15 samples with the maintenance of the ordered mesoporous structure of SBA-15. The presence of these aluminum oxides produced a large number of terminal Al–OH functional groups and Lewis or Brønsted acid sites, which effectively increased the number of active adsorption centers. On the other hand, the increase in aluminum loading blocked the pore channels of the samples. The specific surface area, pore volume and microstructural regularity of the samples were reduced. In addition, excessively increasing the aluminum loading led to the overlapping arrangement of aluminum-oxide compounds on the SBA-15 surface, which could lead to the dehydroxylation and dehydration reactions of the terminal Al–OH functional group with the adjacent -OH group, shifting aluminum to a lower coordination environment. Consequently, the decreases in the effective utilization of terminal Al–OH functional groups and in the total amount of active adsorption centers had been resulted. When the aluminum loading was 10%, the positive and negative factors reached a balance, and then the highest adsorption capacity of 95.7 mg/g_{Al} for As(V) was obtained.

The adsorption kinetics of As(V) on Al_x-SBA-15 followed the pseudo-second-order model and the intraparticle diffusion model, that is, the adsorption process was dominated by chemical adsorption, and the adsorption rate was jointly controlled by film diffusion and intraparticle diffusion. The Al_{10}-SBA-15 adsorbent was desorbed by NaOH solution, and the desorption efficiency could reach 90% within 4 h, which provided a possibility for the subsequent resource utilization of

Table 4 The concentration of coexiting anions in real sample

Real sample	Cl^- (mg/L)	F^- (mg/L)	NO_3^- (mg/L)	SO_4^{2-} (mg/L)	PO_4^{3-} (mg/L)	As (mg/L)
1#	56.8	34.2	67.2	189.3	47.9	1.998
2#	110	29.4	59.1	56.9	51.5	1.242

arsenic. The Al$_{10}$-SBA-15 adsorbent was applied to the actual arsenic-contaminated wastewater with arsenate of 1.998 mg/L and 1.242 mg/L, and the results showed that the treated water samples reached the drinking water standard, indicating that Al$_{10}$-SBA-15 was an adsorbent that can efficiently treat polluted water with low arsenic content.

Author contributions XL performed the experiments and analysis and wrote the main manuscript text. XL and YL guided XL in some characterization. XL and BH helped XL in analyzing XRD and IR images. XH and CL gave some guidance on the means of the analysis of the material. NL and SH guided the research and revised the draft.

Declarations

References

1. J.H. Park, J.H. Lee, S.L. Lee, S.W. Hwang, D.C. Seo, Colloids Surf. A **626**, 127095 (2021). https://doi.org/10.1016/j.colsurfa.2021.127095

2. M.B. Shakoor, R. Nawaz, F. Hussain, M. Raza, S. Ali, M. Rizwan, S.-E. Ahmad, Sci. Total Environ. **601**, 756–769 (2017). https://doi.org/10.1016/j.scitotenv.2017.05.223

3. S. Bibi, M.A. Kamran, J. Sultana, A. Farooqi, Environ. Chem. Lett. **15**, 125–149 (2017)

4. S.F. Wang, D.N. Zhang, X.L. Li, G.Q. Zhang, Y. Wang, X. Wang, M.A. Gomez, Y.F. Jia, J. Hazard. Mater. **360**, 311–318 (2018). https://doi.org/10.1016/j.jhazmat.2018.08.017

5. A. Ortega, I. Oliva, K.E. Contreras, I. González, M.R. Cruz-Díaz, E.P. Rivero, Sep. Purif. Technol. **184**, 319–326 (2017). https://doi.org/10.1016/j.seppur.2017.04.050

6. C.X. Deng, J.J. Wen, Z.W. Li, N.L. Luo, M. Huang, R. Yang, Ecotoxicol. Environ. Saf. **164**, 270–276 (2018). https://doi.org/10.1016/j.ecoenv.2018.08.019

7. V.K. Tchieda, E. D'Amato, A. Chiavola, M. Parisi, A. Chianese, M. Amamra, A. Kanaev, CLEAN-Soil Air Water **44**, 496–505 (2016). https://doi.org/10.1002/clen.201400599

8. T.F. Lin, J.K. Wu, Water Res. **35**, 2049–2057 (2001). https://doi.org/10.1016/S0043-1354(00)00467-X

9. S. Ghosh, R. Prabhakar, S. Samadder, Clean Technol. Environ. Policy **21**, 121–138 (2019)

10. S. Lata, S.R. Samadder, J. Environ. Manage. **166**, 387–406 (2016). https://doi.org/10.1016/j.jenvman.2015.10.039

11. M.J. Yu, X. Li, W.S. Ahn, Microporous Mesoporous Mat. **113**, 197–203 (2008). https://doi.org/10.1016/j.micromeso.2007.11.020

12. W. Li, C.Y. Cao, L.Y. Wu, M.F. Ge, W.G. Song, J. Hazard. Mater. **198**, 143–150 (2011). https://doi.org/10.1016/j.jhazmat.2011.10.025

13. C.Y. Han, H.Y. Li, H.P. Pu, H.L. Yu, L. Deng, S. Huang, Y.M. Luo, Chem. Eng. J. **217**, 1–9 (2013). https://doi.org/10.1016/j.cej.2012.11.087

14. C.Y. Han, H. Liu, H. Chen, L.M. Zhang, G.P. Wan, X. Shan, J.S. Deng, Y.M. Luo, J. Taiwan Inst. Chem. Eng. **65**, 204–211 (2016). https://doi.org/10.1016/j.jtice.2016.05.003

15. H.Y. Chen, S.Y. Fu, L.J. Fu, H.M. Yang, D.L. Chen, Minerals **9**, 264 (2019). https://doi.org/10.3390/min9050264

16. A. Najafi Chermahini, M. Assar, J. Iran, Chem. Soc. **16**, 2045–2053 (2019). https://doi.org/10.1007/s13738-019-01677-4

17. P. Bhange, D.S. Bhange, S. Pradhan, V. Ramaswamy, Appl. Catal. A-Gen. **400**, 176–184 (2011). https://doi.org/10.1016/j.apcata.2011.04.031

18. Q. Zhang, L. Shi, X. Meng, RSC Adv. **6**, 112201–112209 (2016). https://doi.org/10.1039/C6RA18777C

19. A. Prabhu, V. Sudha, M.P. Pachamuthu, B. Sundaravel, S. Bellucci, J. Nanomater. **2022**, 1–10 (2022). https://doi.org/10.1155/2022/2512223

20. B. Boukoussa, R. Hamacha, A. Morsli, A. Bengueddach, Arab. J. Chem. **10**, S2160–S2169 (2017). https://doi.org/10.1016/j.arabjc.2013.07.049

21. Y. Glocheux, A.B. Albadarin, J. Galán, E. Oyedoh, C. Mangwandi, C. Gerente, S.J. Allen, G.M. Walker, Microporous Mesoporous Mat. **198**, 101–114 (2014). https://doi.org/10.1016/j.micromeso.2014.07.020

22. S. Rostamnia, K. Lamei, F. Pourhassan, RSC Adv. **4**, 59626–59631 (2014). https://doi.org/10.1039/c4ra09157d

23. H. Alamgholiloo, S. Rostamnia, Appl. Organomet. Chem. N. Noroozi Pesyan **34**, e5452 (2020). https://doi.org/10.1002/aoc.5452

24. D. Pečar, A. Goršek, Mechanisms React. Kinet. Mech. Catal. **128**, 991–1003 (2019). https://doi.org/10.1007/s11144-019-01674-x

25. V. Chaudhary, S. Sharma, J. Porous Mater. **24**, 741–749 (2017). https://doi.org/10.1007/s10934-016-0311-z

26. S. Rostamnia, X. Liu, D. Zheng, J. Colloid Interface Sci. **432**, 86–91 (2014). https://doi.org/10.1016/j.jcis.2014.06.011

27. S. Rostamnia, T. Rahmani, Appl. Organomet. Chem. **29**, 471–474 (2015). https://doi.org/10.1002/aoc.3319

28. S. Rostamnia, F. Pourhassan, Chin. Chem. Lett. **24**, 401–403 (2013). https://doi.org/10.1016/j.cclet.2013.03.020

29. H.G. Hosseini, E. Doustkhah, M.V. Kirillova, S. Rostamnia, G. Mahmoudi, A. Kirillov, Appl. Catal. A. **548**, 96–102 (2017). https://doi.org/10.1016/j.apcata.2017.07.006

30. Z. Wu, Q.Y. Lu, W.H. Fu, S. Wang, C.B. Liu, N. Xu, D.T. Wang, Y.M. Wang, Z.G. Chen, New J. Chem. **39**, 985–993 (2015). https://doi.org/10.1039/C4NJ01473A

31. P.L. Zhang, Z.F. Wu, T.X. Liu, Z.Q. Li, Eur. J. Inorg. Chem. **2014**, 5577–5584 (2014). https://doi.org/10.1002/ejic.201402511

32. J. Ming, E.W. Shin, J.K. Park, Water Environ. Fed. **2002**, 40–54 (2002). https://doi.org/10.2175/193864702784163263

33. S.F. He, C.Y. Han, H. Wang, W.J. Zhu, S.Y. He, J. Chem. Eng. Data. **60**(5), 1300–1310 (2015). https://doi.org/10.1021/je500978k

34. Z. Talha, C. Bachir, S. Ziri, S. Bellahouel, A. Bengueddach, F. Villièras, M. Pelletier, P.G. Weidler, R. Hamacha **147**, 2116–2126 (2017). https://doi.org/10.1007/s10562-017-2103-8

35. P.T. Huyen, L.T. Nam, T.Q. Vinh, C. Martínez, V. Parvulescu, Catal. Today. **306**, 121–127 (2018). https://doi.org/10.1016/j.cattod.2017.03.040

36. X. Guo, H.S. Shi, W.B. Zhong, H.H. Xiao, X. Liu, T. Yu, C.R. Zhou, Ceram. Int. **46**, 11762–11769 (2020). https://doi.org/10.1016/j.ceramint.2020.01.210

37. H.G. Hosseini, S. Rostamnia, New J. Chem. **42**, 619–627 (2018). https://doi.org/10.1039/C7NJ02742G

38. Y.Y. Zhang, G.H. Wu, Y. Yang, J.Y. Sun, D.E. Zhang, J. Sol-Gel Sci. Technol. **98**, 170–182 (2021). https://doi.org/10.1007/s10971-020-05455-0

39. H.B. Yu, X. Jia, P. Wang, Y. Xiong, W.J. Shan, C.G. Zhang, Z.M. Song, Microporous Mesoporous Mat. **327**, 111432 (2021). https://doi.org/10.1016/j.micromeso.2021.111432

40. S.M. Hafezian, P. Biparva, A. Bekhradnia, S.N. Azizi, Adv. Powder Technol. **32**, 779–790 (2021). https://doi.org/10.1016/j.apt.2021.01.025

41. S. Thangarasu, V. Siva, S. Asath, B.S. Athimoolam, Opt. Quantum Electron. **53**(1), 16 (2021). https://doi.org/10.1007/s11082-021-03146-w

42. J. Wisniewska, I. Sobczak, M. Ziolek, Technology, Catal. Sci. Technol. **11**, 2242–2260 (2021). https://doi.org/10.1039/D0CY02135K

43. C.H. Nguyen, C.-C. Fu, Z.-H. Chen, T.T. Van Tran, S.H. Liu, R.-S. Juang, Microporous Mesoporous Mat. **311**, 110733 (2021). https://doi.org/10.1016/j.micromeso.2020.110733

44. E. Doustkhah, S. Rostamnia, A. Hassankhani, J. Porous Mater. **23**, 549–556 (2015). https://doi.org/10.1007/s10934-015-0108-5

45. B. Hamzaoui, A. Bendjeriou-Sedjerari, E. Pump, E. Abou-Hamad, R. Sougrat, A. Gurinov, K.-W. Huang, D. Gajan, A. Lesage, L. Emsley, Chem. Sci. **7**, 6099–6105 (2016). https://doi.org/10.1039/c6sc01229a

46. Y.N. Zeng, S.X. Liu, Y.Q. Xu, F.A. Zhang, J. Porous Mater. **27**, 659–669 (2020). https://doi.org/10.1007/s10934-019-00841-8

47. I. Rakngam, N. Osakoo, J. Wittayakun, N. Chanlek, A. Pengsawang, N. Sosa, T. Butburee, K. Faungnawakij, P. Khemthong, Microporous Mesoporous Mat. **317**, 110999 (2021). https://doi.org/10.1016/j.micromeso.2021.110999

48. S. Rostamnia, E. Doustkhah, Tetrahedron Lett. **55**, 2508–2512 (2014). https://doi.org/10.1016/j.tetlet.2014.03.019

49. A.S. Andreev, V. Livadaris, J. Phys. Chem. C **121**, 14108–14119 (2017). https://doi.org/10.1021/acs.jpcc.7b02283

50. J.A. van Bokhoven, A.M. Van der Eerden, D.C. Koningsberger, J. Am. Chem. Soc. **125**, 7435–7442 (2003). https://doi.org/10.1021/ja0292905

51. S. Lin, L. Shi, H.P. Zhang, N. Zhang, X.F. Yi, A.M. Zheng, X.B. Li, Microporous Mesoporous Mat. **184**, 151–161 (2014). https://doi.org/10.1016/j.micromeso.2013.10.016

52. A. Sherlala, A. Raman, M.M. Bello, A. Buthiyappan, J. Environ. Manage. **246**, 547–556 (2019). https://doi.org/10.1016/j.jenvman.2019.05.117

53. B. Tanhaei, A. Ayati, M. Lahtinen, M. Sillanpää, Chem. Eng. J. **259**, 1–10 (2015). https://doi.org/10.1016/j.cej.2014.07.109